Geochemical Perspectives Letters

Vivianite-parasymplesite solid solution: A sink for arsenic in ferruginous environments?

J.P.H. Perez, M. Okhrymenko, R. Blukis, V. Roddatis, S. Mayanna, J.F.W. Mosselmans, L.G. Benning

Supplementary Information

The Supplementary Information includes:

- S-1 Elemental Concentration Analysis
- S-2 Material Characterization
- Supplementary Tables S-1 to S-8
- Supplementary Figures S-1 to S-16
- Supplementary Information References

S-1 Elemental Concentration Analysis

After the precipitation of the As-substituted vivianites, an aliquot of the suspension was sampled and added to a 0.3 M HNO_3 solution for the analysis of the total elemental concentration. The liquid phase was obtained by filtering the suspension though a 0.2-µm polycarbonate membrane filter, and then acidified using concentrated HNO_3 (Aristar® for trace analysis). Acidified samples were stored at ~4 °C until analysis. The elemental composition of precipitates was calculated from the difference between the concentrations in the suspension and liquid phase, determined from inductively coupled plasma optical emission spectrometry (ICP-OES, Varian 720ES) as described in our previous study (Perez *et al.*, 2019).

Acidified liquid samples (pH ≈ 2) were diluted gravimetrically in acid-cleaned polypropylene (PP) tubes prior to inductively coupled plasma optical emission spectrometry (ICP-OES) analyses. Sample dilutions were performed using 0.3 M HNO_3 (Merck Suprapur® grade) containing 1 mg g^{-1} Cs as an ionisation buffer to achieve matrix matching with calibration standards prepared from a mixture of single ICP element standards (Merck Certipur®, traceable to NIST reference materials). Scandium (1 µg g^{-1}) was added as an internal standard. Dilution factors were adapted to ensure that analyte solutions were within the concentration range of the matrix-matched calibration standards (linearity criteria $R^2 > 0.9990$) and with final HNO_3 and Cs concentrations of 0.3 M and 1 mg g^{-1}, respectively.

For each analytical session, instrumental stability and drift were monitored using Ar, Cs and Sc at emission wavelengths of 420.067, 459.311 and 335.372 nm for each sample analysis, respectively, as well as regular measurements of a quality control (QC) solution, similar to sample compositions. Instrumental statistical limits of detection (LoD = 3 s.d. above background) or limits of quantification (LoQ = 10 s.d. above background) were determined in each analytical session based on nine repeat analysis of 0.3 M HNO_3 (+1 mg g^{-1} Cs) used for sample dilution.

Concentrations of As, P and Fe in the samples were evaluated using the emission wavelengths of 193.696, 214.914 and 261.382 nm, respectively. The determined LoD values were 0.011 µg g^{-1} for As, 0.022 µg g^{-1} for P and 0.012 µg g^{-1} for Fe. Analytical uncertainties at a 95 % confidence level for concentrations quantified (above LoQ) during this study are ~5 % relative, verified by repeat analyses of a QC solution, which was similar to the sample compositions (Table S-1).

S-2 Material Characterisation

S-2.1 Powder X-ray diffraction (XRD) and Rietveld refinement

Samples for XRD measurements were loaded into glass capillaries (ø = 0.5 mm, Hilgenberg glass capillary no. 50) and sealed with Cristaseal wax (Hawksley & Sons Ltd.) inside the anaerobic chamber. XRD patterns were recorded using a STOE STADI P X-ray diffractometer operated in Debye-Scherrer geometry using Ag $K\alpha_1$ radiation (λ = 0.56087 Å) from a primary beam Ge(111) monochromator and equipped with two DECTRIS MYTHEN2 R 1K position sensitive detectors. Scattered X-rays were collected over the *Q*-range of 0 to ~13.4 $Å^{-1}$. Each sample measurement lasted for 2.5 h, and samples were spun during data collection for improved particle statistics. Rietveld analysis of the XRD patterns was performed using the GSAS-II software (Toby and Von Dreele, 2013). Instrument function parameters were obtained by fitting NIST LaB_6 standard diffraction peaks. The samples were modelled as a single phase vivianite or parasymplesite (*C2*/*m* symmetry) (Mori and Ito, 1950), and considered as a perfect solid solution with P/As site being occupied by either P or As. The background was approximated with ten Chebyschev polynomials. Refined parameters included unit cell, grain size, microstrain, As/P ratio, thermal displacement and atomic position parameters. Grain size was modelled using uniaxial approximation with (001) being the unique axis in accordance with observations with SEM/TEM.

S-2.2 Scanning electron microscopy (SEM)

Samples for SEM were prepared inside an anaerobic chamber by fixing the dried powder samples onto a double-sided carbon tape attached to SEM stubs. Stubs were put inside an anaerobic jar to minimize oxidation during rapid transfer to the SEM, quickly loaded into vacuum sputter coater (BAL-TEC MED 020 Leica Microsystems) and coated (*ca*. 5–8 nm thick) with carbon to avoid charging effects during imaging. SEM images were acquired using a ZEISS Ultra Plus FEG-SEM operated in high vacuum mode at an acceleration voltage of 3 kV with 10 µm aperture size using an InLens secondary electron detector. Elemental analyses of samples were performed at 20 kV with 120 µm aperture size in point and shoot mode using a Thermo Scientific Ultra Dry Energy Dispersive Spectrometry (EDX) detector.

S-2.3 Transmission electron microscopy (TEM)

Dry powder samples were loaded in screw capped sample vials inside the anaerobic chamber and then transported to the sample preparation lab. Samples were ground in ethanol using an agate mortar and pestle, and immediately drop-casted onto a holey amorphous coated carbon copper grid. HAADF-STEM images and EDX maps were recorded using a Thermo Fisher Scientific™ Themis Z (3.1) Scanning Transmission Electron Microscope operated at 300 kV and equipped with a Super-X EDX system, and a Gatan Continuum ER/1065 imaging filter.

S-2.4 X-ray absorption spectroscopy

The pellets were prepared inside the anaerobic chamber at GFZ Potsdam by mixing dry powder samples with cellulose using an agate mortar and pestle. Mixture calculations were performed using XAFSmass software (Klementiev and Chernikov, 2016). Pellets were sealed inside sample holders made of two layers of single-sided 70-µm thick Kapton® polyimide tape. The Kapton-sealed pellet samples were placed inside air-tight headspace crimp vials stored inside an anaerobic jar to prevent oxidation during sample transport to the beamline. The sample vials were immediately

transferred to the glovebox (Ar atmosphere, MBRAUN) upon arrival at the beamline. The Kapton-sealed samples were fixed onto a sample holder provided by the beamline and then transferred to the station using an anaerobic jar.

Fe and As K-edge XAS data were collected at I20-scanning of Diamond Light Source (UK) (Diaz-Moreno *et al.*, 2018). Spectra were recorded at liquid nitrogen (LN_2) temperatures (~77 K) both in transmission and fluorescence mode to a reciprocal space value of ~14.8 $Å^{-1}$. For this, a LN_2 cryostat with a helium convection (Optistat DN2, Oxford Instruments). Fluorescence data was collected using a 64-element Ge solid-state detector equipped with Xspress4. The vertical dimension of the X-ray beam during data collection was 400 µm and the horizontal dimension was 300 µm. To prevent second-order harmonics, rejection mirrors were used. A Si(111) crystal pair ($\Delta E/E = 1.3 \times 10^{-4}$) with a fixed beam exit was used as a monochromator. The maximum in the first derivative of X-ray absorption spectra from Fe and Au foils were used to calibrate the beam at 7112 eV (Fe K-edge) and 11,919 eV (Au L_3 edge), respectively. The XANES region was measured with 0.3 eV steps. Three to four scans were collected for each sample depending on data quality. During the data collection, changes in line shape and peak position indicative of beam-induced redox reactions were examined and, however, no beam damage was observed.

Spectra were aligned, averaged, and background-subtracted using the SIXpack software (Webb, 2005). Shell-by-shell fits of the As K-edge EXAFS spectra were performed from 1 to 4 Å in $R + \Delta R$-space using SIXpack software, based on algorithms derived from IFEFFIT (Newville, 2001). The fits typically included the interatomic distance (R), the coordination number (CN), the mean squared atomic displacement parameter (σ^2), and the change in threshold energy (ΔE_0) for one sample. Phase and amplitude functions for single and multiple scattering paths were calculated using FEFF6 (Rehr *et al.*, 1992) and As atomic pair paths (*i.e.* As-O, As-O-O and As-Fe/Fe-As) were derived from the crystal structure of paths from scorodite (Kitahama *et al.*, 1975). In the preliminary shell-by-shell fits, CN and σ^2 were found to be highly correlated, producing high fit-derived standard errors in these fitting parameters. The σ^2 values of the As-Fe path was therefore constrained to 0.004 (Muehe *et al.*, 2016) to reduce the high degree of correlations. Consistent with previous works (Paktunc *et al.*, 2008; Mikutta *et al.*, 2010), the passive electron reduction parameter (S_0^2) in each fit was set to 1.0. The goodness-of-fit was assessed based on the R-factor, which is defined as the mean square difference between the fit and the data on a point-by-point basis: R-factor = $\sum_i (\text{data}_i - \text{fit}_i)^2 / \sum_i (\text{data}_i)^2$. An R-factor of <0.05 is considered to reflect a reasonable fit (Kelly *et al.*, 2008).

S-2.5 Infrared spectroscopy and spectra interpretation

Dry powder samples were placed inside 2-mL glass vial and then put in crimp capped glass vials to prevent oxidation during transport. Sample vials were opened just before each spectrum was collected. Spectra were acquired using a Nicolet iS5 Fourier Transform infrared spectrometer (Thermo Fisher Scientific™) equipped with a diamond attenuated total reflection (ATR) accessory (iD7 ATR, Thermo Fisher Scientific™). Spectra were collected over the 4000–400 cm^{-1} range with a resolution of 4 cm^{-1} by averaging 64 individual scans. Baseline correction and peak fitting were done using the OMNIC software (Thermo Fisher Scientific™). For integrated area calculations, bands between ~1200 to ~600 cm^{-1} (*i.e.* PO_4^{3-} and AsO_4^{3-} stretching regions) were fitted using a Gauss-Lorentzian function (Gauss amount ≥ 0.7) and the minimum number of component bands possible.

Interpretation of the phosphate [v(PO₄)] and arsenate [v(AsO₄)] stretching regions. As-free vivianite is characterized by three distinct bands at 1035, 966 and 936 cm^{-1}, assigned antisymmetric (ν_3) and symmetric (ν_1) P-O stretching vibrations (Frost *et al.*, 2002). Parasymplesite, on the other hand, is characterized by a sharp band at 770 cm^{-1} with a prominent shoulder at 792 cm^{-1} both arising from As-O antisymmetric stretching vibrations (ν_3) (Frost *et al.*, 2003). The strong band at 806 cm^{-1} in vivianite and 816 cm^{-1} in parasymplesite are attributed to the water librational mode, arising from lattice water molecules.

Interpretation of the water hydroxyl stretching v(OH) and water HOH bending δ(HOH) regions. There are two distinct types of lattice water molecules (O_w1 and O_w2) in the crystal structure of vivianite arsenates that form an intricate network of hydrogen bonds (see Fig. S-1). Type-1 H_2O molecules refer to those found in the Fe1 site (O_W1), which form strong H-bonds by donating their protons to oxygen atoms of adjacent PO_4^{3-} or AsO_4^{3-} tetrahedra in the same layer (Capitelli *et al.*, 2012). Meanwhile, type-2 H_2O molecules in the Fe2 site (O_W2) form strong H-bonds with oxygen atoms of adjacent PO_4^{3-} or AsO_4^{3-} tetrahedra, as well as weaker H-bonds by donating their proton towards other

H_2O molecules in the next layer (*i.e.* lateral connection) (Bartl, 1989). The strength of these H-bonds is reflected in the ν(OH) region. Weakly H-bonded H_2O molecules (shorter H-bond length) in As(V)-substituted vivianites can be attributed to the narrow band at ~3400 cm^{-1} in the IR spectra, while the broad band at ~3100 cm^{-1} corresponds to strongly H-bonded water molecules (longer H-bond length; inset, Fig. S-10) (Frost *et al.*, 2002, 2003). It must be noted, however, that the interpretation of the ν(OH) and δ(HOH) regions can be complicated, as seen from our IR analysis of (partially) deuterated vivianite.

In partially deuterated vivianite, ν(OH) modes between 2700 and 3500 cm^{-1} partially move to between 2100 and 2600 cm^{-1}; however, the shape of the deuterated peaks is very different (Fig. S-15). In deuterated vivianite, the peaks can be fitted with only four Voigt functions (two symmetric and two antisymmetric ν(OH) modes; Fig. S-16a). Voigt 4 is very broad and therefore most likely contain contribution from adsorbed water that was not removed by drying properly. The shapes of the peaks may not be perfectly describable with Voigt functions; however, this is not an uncommon feature in ν(OH) bands of minerals (Ratajczak and Yaremko, 2000). The very different shape of ν(OH) bands of protic vivianite indicate additional contributions to the absorption of peaks of protic water by additional components. The most likely additions are combination bands that have enhanced intensity due to Fermi resonance as has been observed in previous studies of hydrated phosphates (Šoptrajanov *et al.*, 2002). Such Fermi resonance enhanced bands make interpretation and peak assignment in the ν(OH) region very complicated.

Vivianite contains two distinct water molecules; therefore, vivianite IR spectrum should have only two peaks in the δ(HOH) region near 1600 cm^{-1}. However, as observed in this work as well as others (Frost *et al.*, 2002, 2003), the δ(HOH) region can only be described with at least 3 distinct peaks. However, in the deuterated vivianite (Fig. S-16b), only two peaks are needed, indicating this extra peak does not originate from some δ(HOH). It can be observed that there is a very strong water libration mode at about half the frequency of the δ(HOH) modes. Water libration mode has a very broad peak, like the one observed in the bending region. Therefore, this additional peak is most likely an overtone of water libration mode. As libration involves the movement of the entire molecule, the effect of deuteration has little effect on its frequency (change of 18 *vs*. 19 or 20 g mol^{-1}, 5 to 10 % change). By applying Morse oscillator model, water libration mode can be described as having fundamental frequency $\omega_0 = 845$ cm^{-1} and anharmonicity parameter $\chi = 0.024$. There can even be seen a potential very small hint of a broad peak at 2287 cm^{-1} which would correspond to the second overtone of the same vibration mode, and would be consistent with predictions form the Morse model.

S-2.6 Geochemical modelling

Geochemical calculations were carried out in The Geochemist's Workbench® (GWB) 2023 (Bethke, 2010) using the MINTEQ database. Since the solubility constant (K_{sp}) of parasymplesite ($pK_{sp} = 33.25$) were missing, the data reported by Johnston and Singer (2007) were added in the MINTEQ database. We also modified the pK_{sp} of vivianite to 35.8 based on the solubility data from (Al-Borno and Tomson, 1994) in the database. Thermodynamically stable iron (oxyhydr)oxides (*e.g.*, hematite, magnetite, goethite, lepidocrocite) were suppressed successively for calculations involving thermodynamically metastable Fe phases. The reaction of HS^- and SO_4^{2-} was also decoupled to model ferruginous (*i.e.* anoxic, non-sulfidic) conditions.

S-2.7 Calculation of the degree of substitution in the As-vivianite samples

The extent of As incorporation in As-vivianites (mole fraction of AsO_4^{3-} substituted, x_{AsO4}) was estimated using different characterization methods.

ICP-OES analysis. The x_{AsO4} of the As-vivianites was determined using the formula:

$$x_{AsO_4} = \frac{[AsO_4^{3-}]_{solid}}{[AsO_4^{3-}]_{solid} + [PO_4^{3-}]_{solid}} \quad \text{(eq. S-1)}$$

$$x_{AsO_4} = \frac{([AsO_4^{3-}]_{susp} - [AsO_4^{3-}]_{snt})}{([AsO_4^{3-}]_{susp} - [AsO_4^{3-}]_{snt}) + ([PO_4^{3-}]_{susp} - [PO_4^{3-}]_{snt})} \quad \text{(eq. S-2)}$$

where: $[YO_4^{3-}]_{solid}$ concentration of AsO_4^{3-} or PO_4^{3-} in the solids (*Y* representing As or P), calculated from the difference in their concentration in the acidified suspension and supernatant (see Text S-1);
$[YO_4^{3-}]_{susp}$ concentration of AsO_4^{3-} or PO_4^{3-} in the acidified mineral suspension;
$[YO_4^{3-}]_{snt}$ concentration of AsO_4^{3-} or PO_4^{3-} in the acidified supernatant.

Rietveld refinement of XRD data. The x_{AsO4} of the As-vivianites was obtained from the Rietveld refinement of the XRD patterns (see Text S-2.1). In brief, two atoms (*i.e.* As and P) were included in the crystal structure, and were set as equivalent during refinement, forcing both atoms to have the same *x*, *y*, *z* positions and thermal displacement. The site occupancy was refined by constraining the sum of the fraction of As and P to 1 (*i.e.* $f_{As} + f_P = 1$). Only one phase was used during the refinement to reflect a true solid solution, and not just a mixture of the end-members vivianite and parasymplesite. Refinements showed that a two end-member phase model was found to be inconsistent with the XRD data.

SEM-EDX analysis. The x_{AsO4} of As-vivianites was estimated (semi-quantitatively) based from the EDX spot analysis of representative As-vivianite particles (three particles for each sample, with at least six analysis spots *per* particle). The x_{AsO4} was calculated *per* spot as follows:

$$x_{AsO_4} = \frac{As_{at.\,\%}}{As_{at.\,\%} + P_{at.\,\%}} \quad \text{(eq. S-3)}$$

where: $As_{at.\,\%}$ atomic ratio of As;
$P_{at.\,\%}$ atomic ratio of P.

The x_{AsO4} was calculated and then averaged *per* particle, which was then used to get the mean value of x_{AsO4} from the three representative As-vivianite particle.

LCF analysis of Fe-K edge EXAFS. The x_{AsO4} in As-vivianites was estimated using linear combination fitting (LCF) analysis of the k^3-weighted Fe K-edge EXAFS spectra of the samples. LCF analyses were performed with SIXpack software over the *k*-range of 2 to 12.5 $Å^{-1}$ using the spectra of the end-members parasymplesite and vivianite.

PCA analysis of IR spectra. Principal component analysis (PCA) (Vandeginste *et al.*, 1998) was used to determine x_{AsO4} in the vivianite samples. PCA was performed using an in-house code written in Igor Pro v. 8.04. All IR spectra were normalized to total area of 1 before analysis.

Supplementary Tables

Table S-1 ICP-OES data for quality control solutions (QC) that were prepared from single element standard solutions (Merck Certipur®) to achieve chemical compositions similar to the experimental sample solutions. The mean results of *n* replicate analyses are given together with the standard deviation (s.d.) and relative standard deviation (RSD) (s.d. represents 68 % of the population, 2 s.d. represents 95 % of the population). The measured deviation from the reference value is a quantitative estimation of accuracy.

	As (mg L^{-1})	P (mg L^{-1})	Fe (mg L^{-1})
Wavelength (nm)	193.696	214.914	261.382
Instrumental limits			
Limit of detection (LoD)	0.011	0.022	0.012
Limit of quantification (LoQ)	0.032	0.048	0.022
Quality control			
QC verify (n = 6)			
Mean	0.327	2.17	4.26
s.d.	0.007	0.06	0.07
RSD	2.21 %	2.63 %	1.75 %
2RSD	4.42 %	5.27 %	3.50 %
Reference value	0.310	2.04	4.08
Measured deviation from reference value	5.74 %	6.05 %	4.39 %

Table S-2 Mineral saturation indices of vivianite, parasymplesite, amorphous $Fe(OH)_2$ and crystalline $Fe(OH)_2$ based on the elemental composition of the starting solutions used in the precipitation experiments.

Mole fraction AsO_4^{3-}	Concentration (mM)			Saturation indices			
	Fe^{2+}	PO_4^{3-}	AsO_4^{3-}	Vivianite	Parasymplesite	$Fe(OH)_2$, am.	$Fe(OH)_2$, cryst.
0	12.9	9.04	<0.01	10.8	-	-1.93	-1.34
0.22	13.1	6.39	2.11	10.7	9.80	-1.87	-1.27
0.48	12.8	4.02	4.02	10.4	10.6	-1.79	-1.19
0.71	13.1	2.09	6.32	9.94	11.2	-1.72	-1.12
0.82	12.7	1.37	6.67	9.59	11.2	-1.71	-1.11
0.90	12.9	0.74	7.44	9.09	11.4	-1.68	-1.08
0.95	12.3	0.38	7.37	8.51	11.4	-1.69	-1.09
1	13.1	<0.06	8.17	-	11.6	-1.66	-1.06

Table S-3 Elemental concentration (mM) and removal efficiencies (%) of Fe, P and As in the aqueous phase during aging of the mineral suspensions.

Mole fraction AsO_4^3	P				As				Fe			
	Conc. (mM)		Removal (%)		Conc. (mM)		Removal (%)		Conc. (mM)		Removal (%)	
	1 h	24 h	1 h	24 h	1 h	24 h	1 h	24 h	1 h	24 h	1 h	24 h
0	0.249	0.257	97.2	97.1	<0.002	<0.002	-	-	0.93	0.98	92.8	92.6
0.22	0.021	0.027	99.7	99.7	0.004	0.010	99.8	99.6	0.55	0.55	95.8	96.7
0.48	0.016	0.024	99.6	99.4	0.003	0.028	99.9	99.3	0.58	0.56	95.5	95.6
0.71	0.003	0.010	99.7	99.5	0.012	0.033	99.8	99.5	0.64	0.63	95.1	95.3
0.82	0.005	0.015	99.6	98.9	0.005	0.159	99.9	97.7	0.59	0.66	95.3	94.8
0.90	0.001	0.020	99.2	97.3	0.011	0.137	99.8	98.2	0.83	0.89	93.6	93.0
0.95	0.001	0.002	98.4	99.4	0.012	0.030	99.8	99.6	0.68	0.69	94.5	94.5
1	<0.001	<0.001	-	-	0.446	0.781	94.5	90.3	2.55	2.14	80.5	83.2

Table S-4 Mole fraction (x) of As-substitution in vivianite samples. Calculated standard errors are in parenthesis.

Nominal value	Calculated value				
	ICP-OES[a]	XRD[b]	SEM-EDX[c]	EXAFS[d]	IR-PCA[e]
0	-	-	-	-	-
0.25	0.22 (0.05)	0.19	-	0.29 (0.01)	0.22
0.50	0.48 (0.09)	0.43	0.37 (0.03)	0.49 (0.02)	0.44
0.75	0.71 (0.08)	0.63	-	-	0.68
0.83	0.82 (0.08)	0.81	-	-	0.77
0.91	0.90 (0.07)	0.82	-	0.93 (0.02)	0.85
0.95	0.95 (0.08)	0.84	0.97 (0.01)	-	0.92
1	-	-	-	-	-

Note: Calculated standard errors are based on the following: (a) analytical uncertainties based on repeat analysis (n = 8) of quality control solutions (see Table S-1); (b) Rietveld refinement analysis of the XRD data; (c) EDX quantification on from different spots (n = 6); (d) fit-derived errors from the linear combination (LCF) fitting analysis of the Fe K-edge EXAFS spectra of parasymplesite and vivianite (see Table 1 in main manuscript); and (e) PCA analysis of the IR spectra.

Table S-5 Refined lattice parameters of As-substituted vivianites (x = mole fraction of substituted AsO_4^{3-}) obtained from Rietveld analysis of the XRD patterns.

Sample	a (Å)	b (Å)	c (Å)	β (°)	Volume (Å^3)	R_{wp} (%)
Vivianite	10.0965	13.4466	4.7112	104.306	619.781	4.49
x = 0.22	10.1477	13.4723	4.7307	104.435	626.435	4.55
x = 0.48	10.2122	13.4895	4.7441	104.625	632.359	4.62
x = 0.71	10.2652	13.5305	4.7692	104.704	640.711	4.97
x = 0.82	10.2878	13.5497	4.7787	104.749	644.749	3.89
x = 0.90	10.3007	13.5550	4.7825	104.765	645.702	4.33
x = 0.95	10.3114	13.5581	4.7858	104.777	646.935	4.12
Parasymplesite	10.3204	13.5684	4.7887	104.806	648.306	6.44

Table S-6 LCF results and statistics of Fe K-edge k^3-weighted $\chi(k)$ EXAFS spectra of As-substituted vivianites. Fitting was done between 2 and 12.5 Å^{-1} using the spectra of the end-members.

AsO_4^{3-} substitution (mole fraction, *x*)	Weights		Sum	Red. χ2	R-factor
	Vivianite	Parasymplesite			
0.22	0.722 (0.014)	0.295 (0.014)	1.017	0.061	0.008
0.48	0.493 (0.019)	0.480 (0.020)	0.972	0.119	0.017
0.90	0.072 (0.019)	0.980 (0.020)	1.052	0.120	0.015

Table S-7 Summary of As K-edge EXAFS shell-by-shell fitting results of the As(V)-substituted vivianites (x = 0.22, 0.48, 0.90) and parasymplesite.

Sample	Atomic pairs	CN	*R* (Å)	σ^2 (Å^2)	ΔE_0 (eV)	R-factor
Parasymplesite	As-O	6.1 (0.6)	1.69 (0.01)	0.005 (0.001)	4.0 (1.5)	0.019
	As-O-O	*12*	1.82(R_{As-O}) = *3.07*	σ^2 (As-O)		
	As-Fe1	3.1 (0.7)	3.30 (0.02)	*0.004*		
	As-Fe2	2.4 (0.1)	3.46 (0.04)	σ^2 (As-Fe1)		
x = 0.22	As-O	5.3 (0.5)	1.69 (0.01)	0.004 (0.001)	4.6 (1.4)	0.018
	As-O-O	*12*	1.82(R_{As-O}) = *3.08*	σ^2 (As-O)		
	As-Fe1	3.0 (0.6)	3.31 (0.02)	*0.004*		
	As-Fe2	2.4 (0.7)	3.47 (0.03)	σ^2 (As-Fe1)		
x = 0.48	As-O	5.7 (0.6)	1.69 (0.01)	0.004 (0.001)	4.5 (1.5)	0.020
	As-O-O	*12*	1.82(R_{As-O}) = *3.08*	σ^2 (As-O)		
	As-Fe1	3.1 (0.7)	3.30 (0.02)	*0.004*		
	As-Fe2	2.4 (0.8)	3.47 (0.02)	σ^2 (As-Fe1)		
x = 0.90	As-O	5.3 (0.5)	1.69 (0.01)	0.002 (0.001)	4.7 (1.5)	0.018
	As-O-O	*12*	1.82(R_{As-O}) = *3.08*	σ^2 (As-O)		
	As-Fe1	3.2 (0.6)	3.30 (0.02)	*0.004*		
	As-Fe2	2.3 (0.8)	3.47 (0.02)	σ^2 (As-Fe1)		

Note: Variables included in the fit: CN, coordination number; *R*, interatomic distance; σ^2, mean-squared atomic displacement; and ΔE_0, change in threshold energy. Fitting parameters allowed to float are accompanied by fit-determined standard errors in parenthesis while constrained parameters appear in italics. The passive electron reduction factor (S_0^2) was fixed at 1.0. The multiple scattering As-O-O path was constrained geometrically to the single scattering As-O path (R_{As-O-O} = 1.82 × R_{As-O}). The σ^2(As-Fe) values were set to best value found empirically. All fits were carried out from 1 to 3.5 Å in $R + \Delta R$-space. The number of independent points (N_{IDP}) in the fits was 16.5 and the number of variables (N_{Var}) was 8.

Table S-8 IR bands assignments (cm^{-1}) of the As-substituted vivianites (x = mole fraction of substituted AsO_4) and their respective end-members.

Sample	Suggested band assignment					
	OH stretching	HOH bending	PO_4 stretching	AsO_4 stretching	H_2O libration	Outplane bends
Vivianite	3473, 3114	1665, 1614	1035, 966, 936	-	806	666
x = 0.22	3467, 3112	1665, 1615	1029, 967, 937	786	810	666
x = 0.48	3462, 3104	1665, 1615	1076, 1028, 970, 937	779	817	661
x = 0.71	3459, 3084	1665, 1618	1076, 1029, 980, 936	793, 773	816	654
x = 0.82	3459, 3084	1665, 1619	1076, 1036, 1024, 981, 935	794, 773	817	654
x = 0.90	3459, 3084	1663, 1619	1078, 1041, 1022, 981, 936	793, 772	817	651
x = 0.95	3459, 3082	1662, 1619	1043, 1021, 982	792, 770	816	651
Parasymplesite	3459, 3082	1661, 1620	-	792, 770	816	650

References used for band assignments: Nakamoto (1986), Socrates (2004), Frost *et al.* (2002, 2003), Myneni *et al.* (1998).

Supplementary Figures

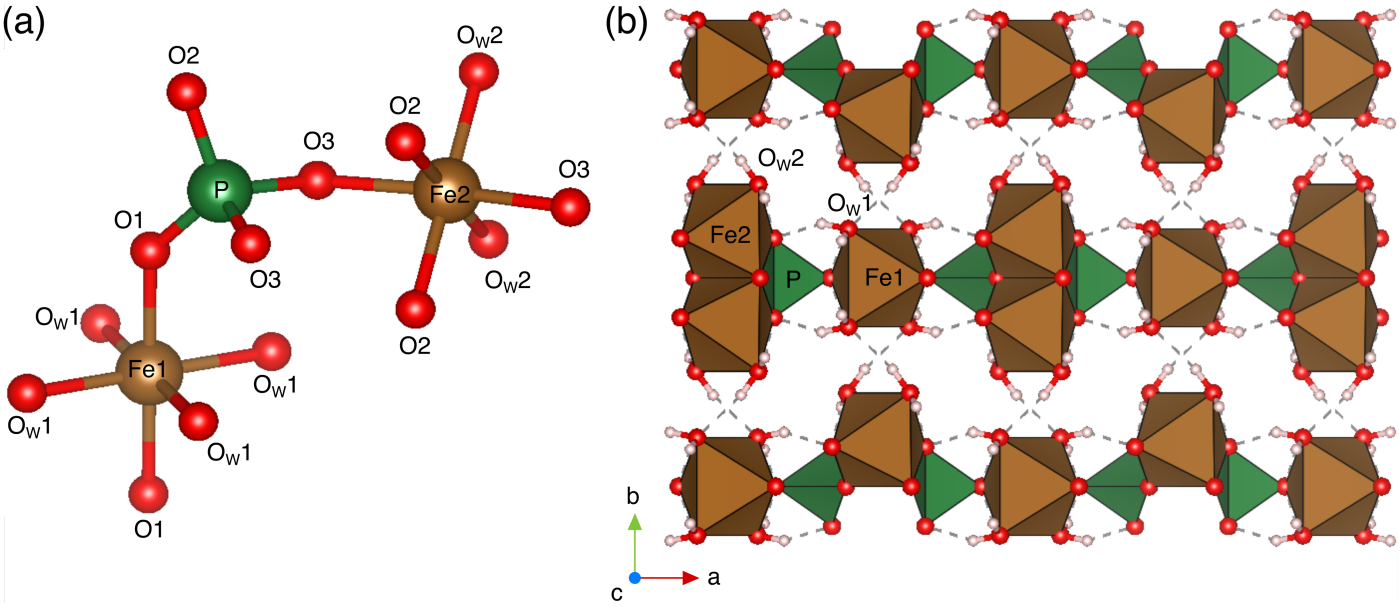

Figure S-1 **(a)** Coordination environment around the Fe1, Fe2 and P sites in the vivianite crystal. Hydrogen atoms were omitted for clarity. **(b)** Crystal structure of vivianite viewed in the *ab* plane showing layers of single Fe1 and edge-sharing Fe2 octahedra (brown) linked by phosphate tetrahedra (green). These layers are held together by hydrogen bonds (dashed lines). Oxygen and hydrogen atoms are indicated in red and pink, with O_w indicating oxygen atoms from water molecules. The local coordination environment and crystal structure were drawn using the VESTA software (Momma and Izumi, 2008) based on the crystallographic information by Capitelli *et al.* (2012).

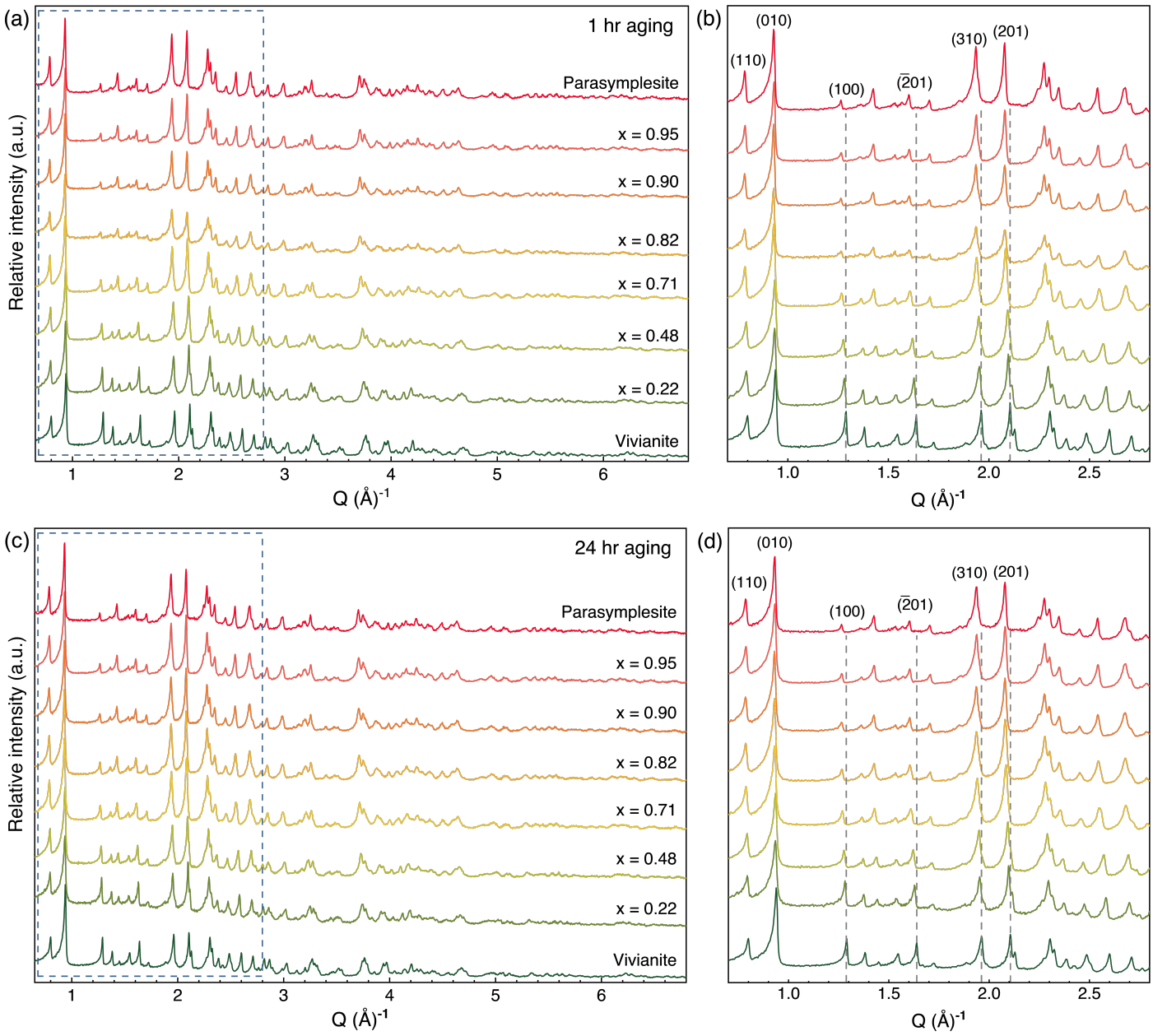

Figure S-2 **(a, c)** Full XRD patterns of the As-substituted vivianites (x = mole fraction of substituted AsO_4^{3-}) plotted in Q-space ($Q = 2\pi/d_{hkl}$) after aging for 1 and 24 h. **(b, d)** Enlarged XRD patterns from **(a)** and **(c)** as indicated by dashed rectangle. Dashed gray lines show the displacement in selected lattice planes in vivianite due to the substitution of AsO_4^{3-} for PO_4^{3-}.

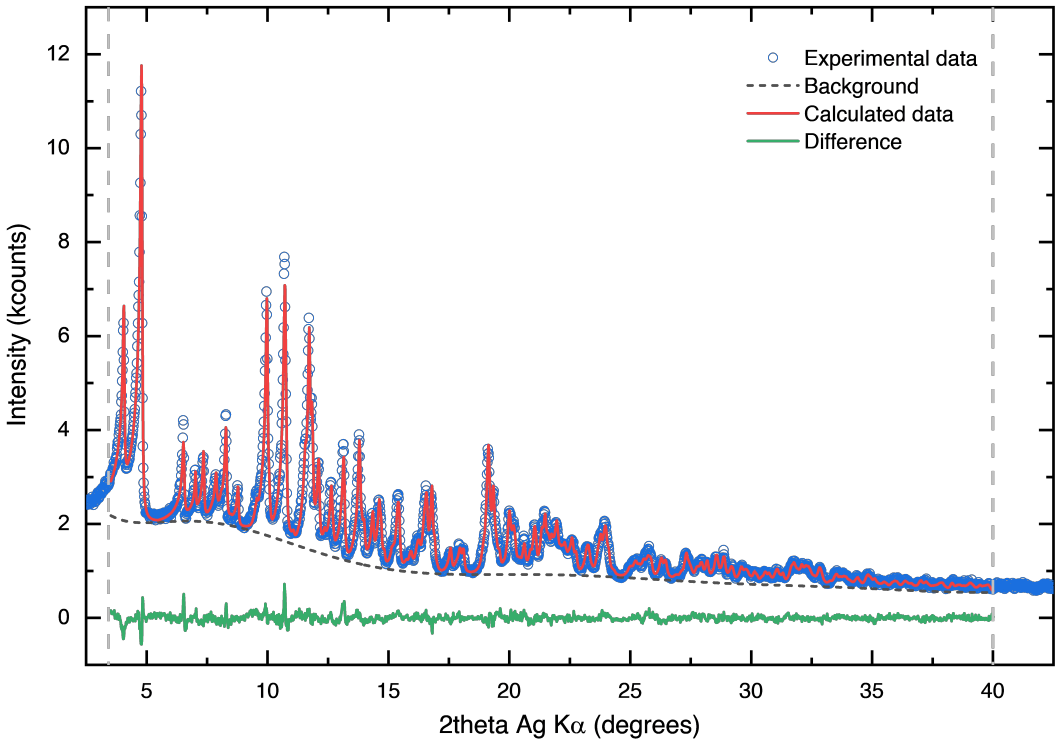

Figure S-3 Sample Rietveld refinement profile of As-substituted vivianite (x = 0.48). Refinement was performed using $C2/m$ vivianite and parasymplesite in the range of 3.5 to 40° 2θ (Ag Kα).

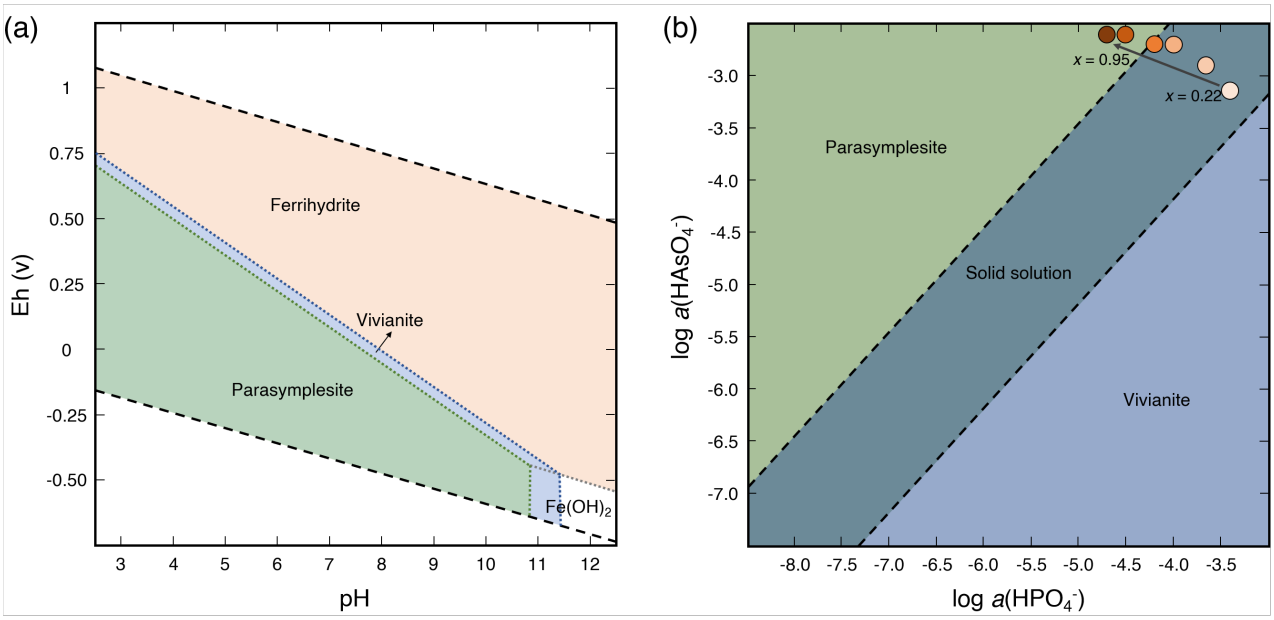

Figure S-4 Geochemical modelling results from Geochemist Workbench (Bethke, 2010) using the MINTEQ database: **(a)** Eh-pH diagram of the Fe-P-As-H_2O system at 25 °C which shows the overlap of the predominance fields of vivianite and parasymplesite and thus indicating a potential solid solution. **(b)** Mineral stabilities in the Fe-P-As-H_2O system at 25 °C. Coloured circles represent the As-substituted vivianites (x = mole fraction of substituted AsO_4^{3-}) synthesized in this study.

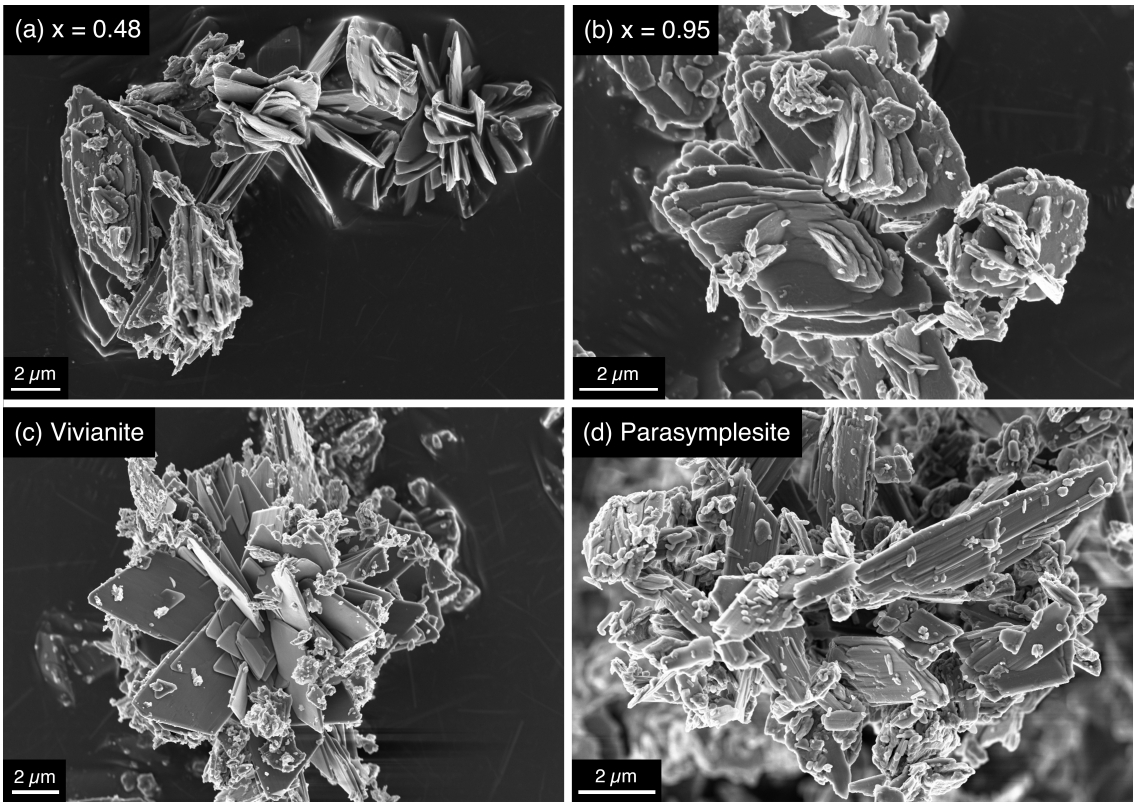

Figure S-5 SEM images of As-vivianites (x = mole fraction of substituted AsO_4^{3-}): **(a)** x = 0.48 and **(b)** x = 0.95, and the end-members **(c)** vivianite (x = 0) and **(d)** parasymplesite (x = 1).

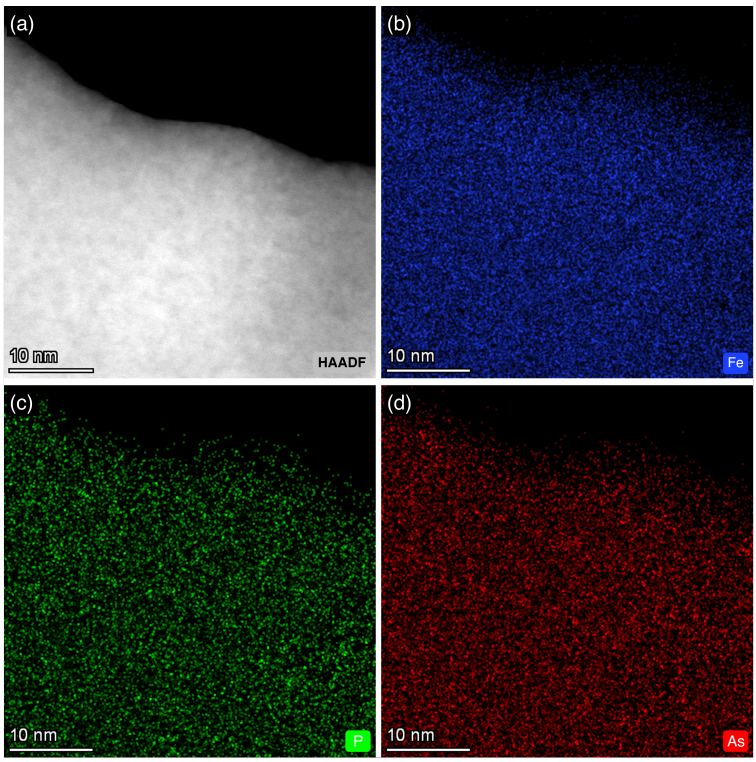

Figure S-6 **(a)** HAADF-STEM image of As-substituted vivianite (x = 0.48) and the corresponding EDX maps: **(b)** Fe (blue); **(c)** P (green); and **(d)** As (red).

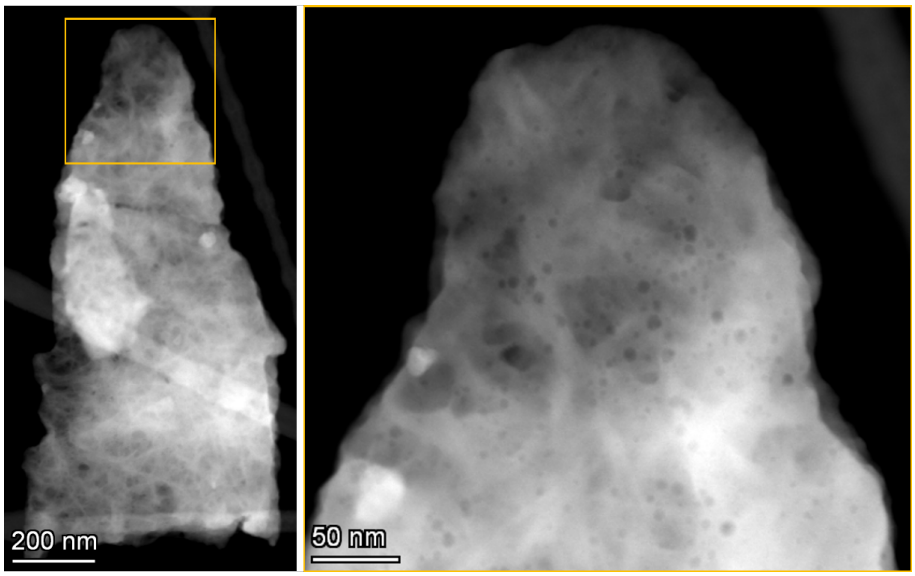

Figure S-7 **(Left)** HAADF-STEM image of As-substituted vivianite (x = 0.48) showing beam-induced changes in the crystal. **(Right)** Magnified HAADF-STEM image of the yellow marked area on the left.

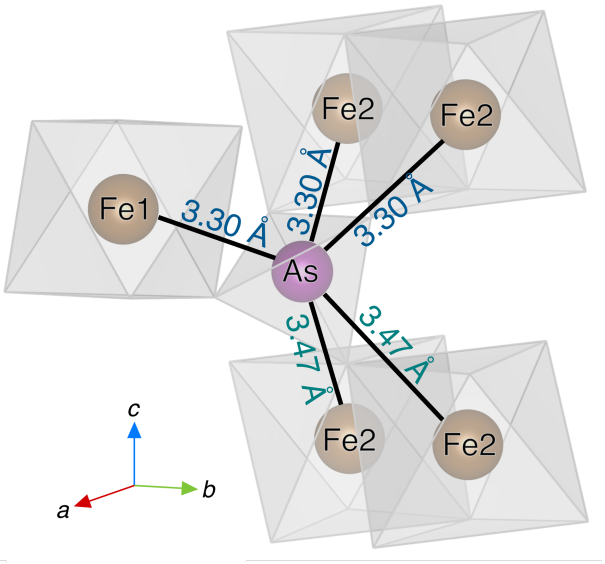

Figure S-8 Local bonding environment of tetrahedral AsO_4^{3-} around the Fe octahedra in parasymplesite showing the two As-Fe interatomic correlations: (i) CN = 3, R = 3.30 Å; and (ii) CN = 2, R = 3.47 Å.

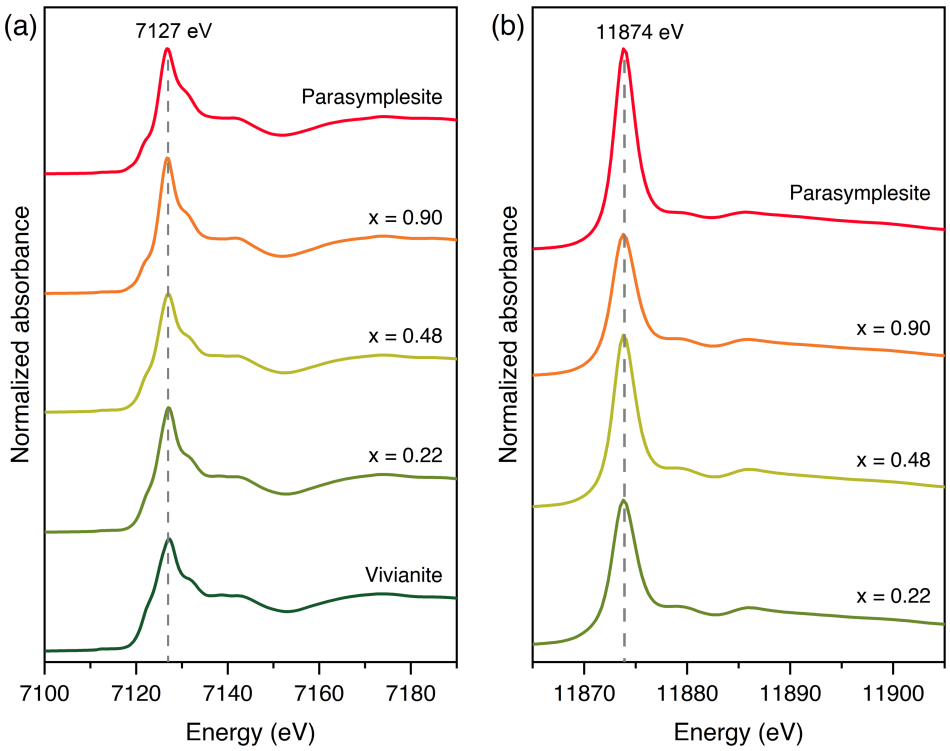

Figure S-9 **(a)** Fe and **(b)** As K-edge XANES spectra of the vivianite, parasymplesite and As(V)-substituted vivianites (x = 0.22, 0.48, 0.98).

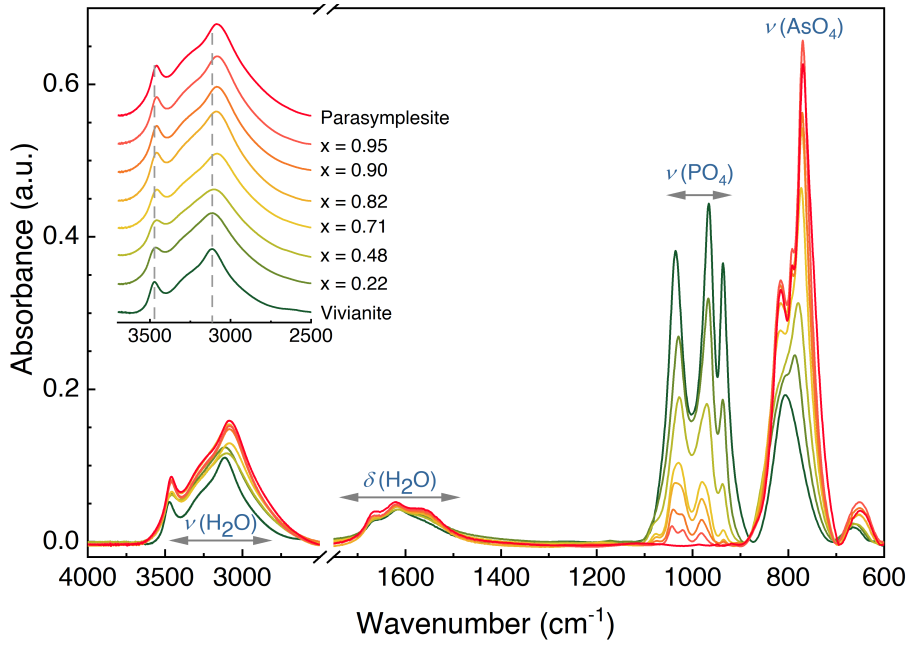

Figure S-10 IR absorption spectra of the As(V)-substituted vivianites (x = mole fraction of substituted AsO_4). Inset: Stacked spectra of the OH stretching region [ν(OH)] showing the positions of weakly and strongly hydrogen bonded H_2O at ~3400 and ~3100 cm^{-1}, respectively.

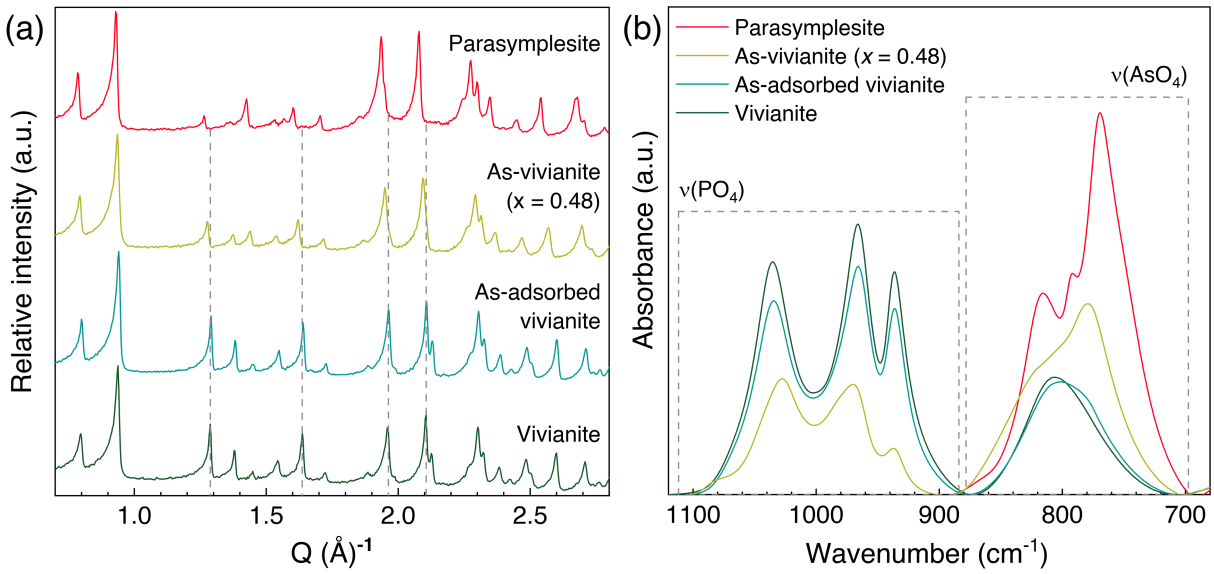

Figure S-11 Comparison between As-vivianite (*i.e.* structurally incorporated; $x = 0.48$), As-adsorbed vivianite (initial [As] = 4 mM, reaction time = 24 h) and the mineral end members vivianite and parasymplesite: **(a)** Zoomed XRD patterns in the Q-range of 0.7 to 2.8 Å. Dashed grey lines indicate vivianite reflections that represent lattice planes affected by As incorporation in vivianite. **(b)** FTIR spectra showing the clear difference in the $\nu(AsO_4)$ band of As-vivianite and As-adsorbed onto vivianite.

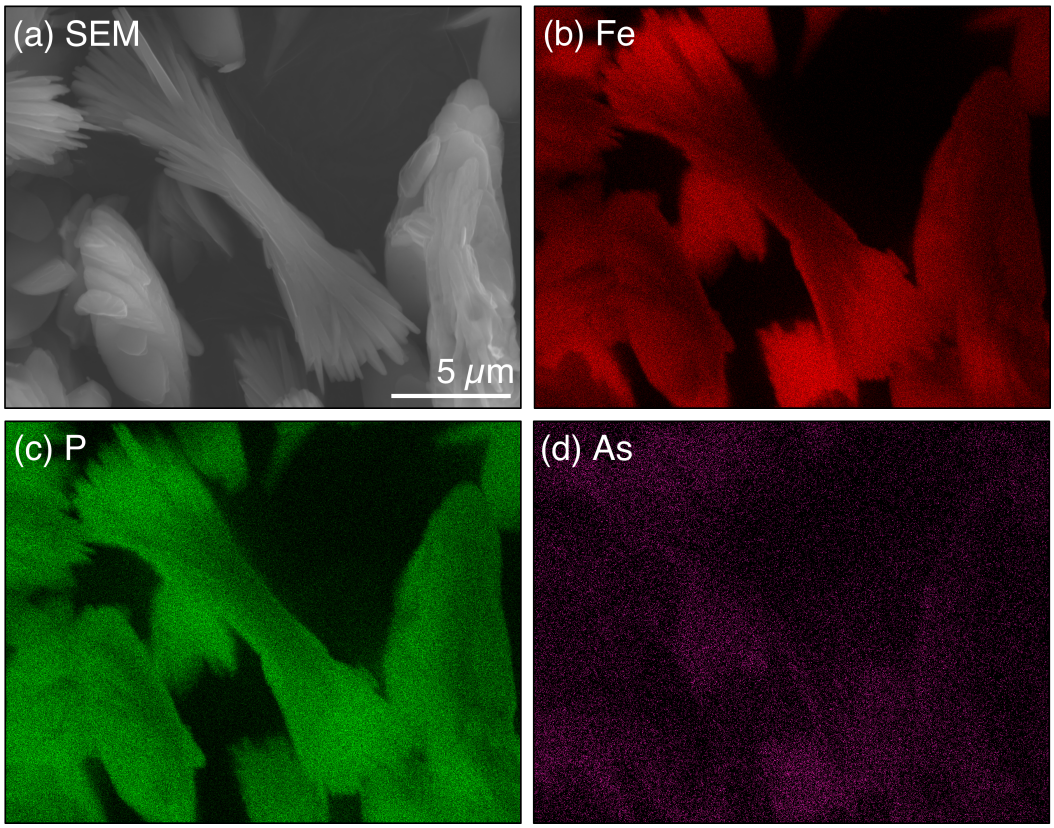

Figure S-12 **(a)** SEM image of pure vivianite ($[Fe]_{viv}$ = 12 mM) reacted with 4 mM As(V) at pH 7 for 24 h (comparable to the 48 mol % As-vivianite). The corresponding EDX maps of As-adsorbed vivianite: **(b)** Fe (red); **(c)** P (green); and **(d)** As (magenta).

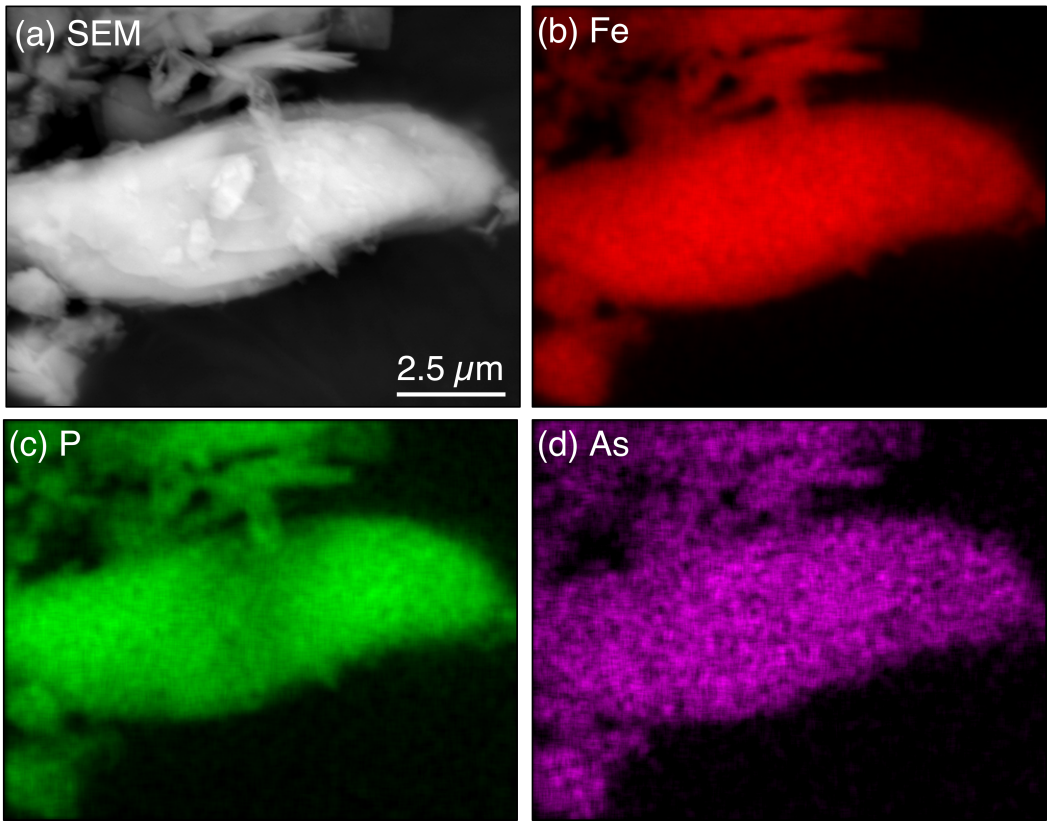

Figure S-13 **(a)** SEM image of 48 mol % As-vivianite and the corresponding EDX maps: **(b)** Fe (red); **(c)** P (green); and **(d)** As (magenta).

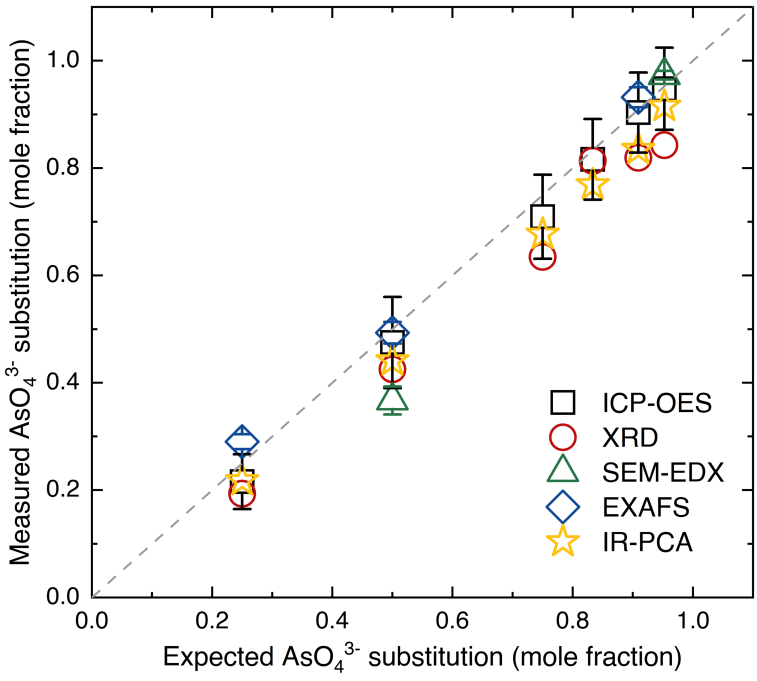

Figure S-14 Comparison of different characterization techniques used in this study for the quantification of As(V)-substitution in vivianite (see Text S-2.7 for more information). Error bars represent: (i) ICP, analytical uncertainties based on repeat analysis (n = 8) of quality control solutions (see Table S-4); (ii) XRD, Rietveld refinement analysis; (iii) SEM-EDX, quantification of different sample spots (n = 6) from representative particles (n = 3); (iv) EXAFS, LCF fit-derived errors (see Table S-6); and (v) PCA analysis of the IR spectra.

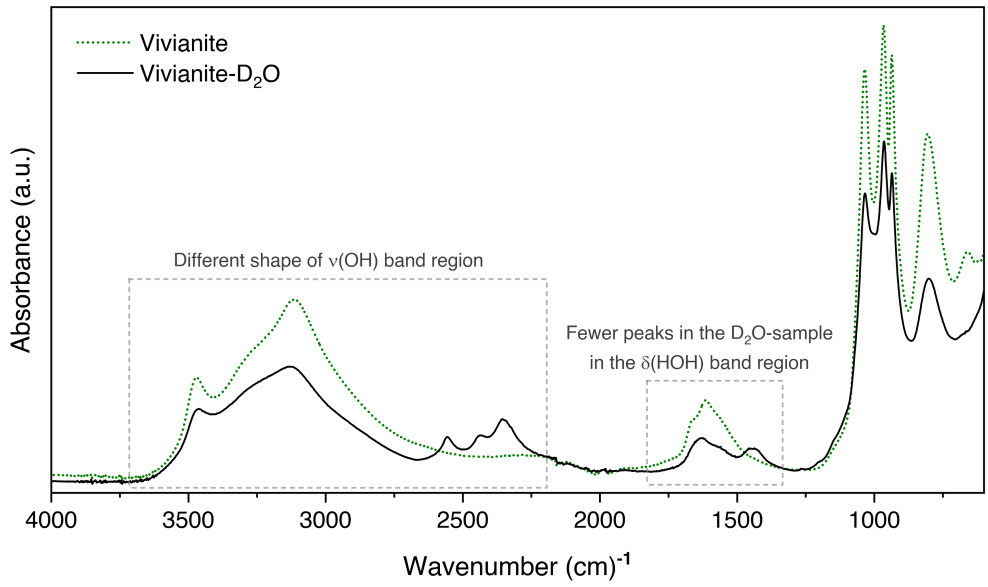

Figure S-15 IR spectra of vivianite and a partially deuterated vivianite. Vibrations involving hydrogen are shifted to lower wavenumbers.

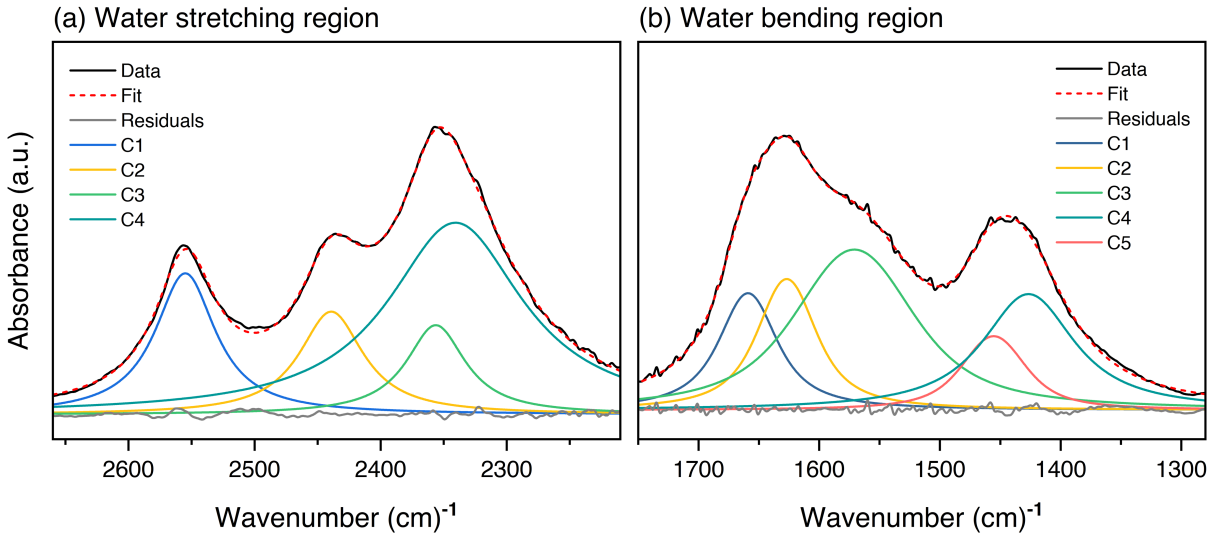

Figure S-16 **(a)** Deuterated water stretching region of partially deuterated vivianite. Only four Voigt curves are needed to achieve a good fit as expected for two distinct water bonding environments. **(b)** Bending region multi-Voigt fit of partially deuterated vivianite. Three peaks were used to fit the bending region of the protic and the two were used to fit the deuterated vivianite. Voigts 1, 2, 4 and 5 correspond to structural water bending modes. Voigt 3 may partially correspond to adsorbed water (wet sample); however, the enormous area disparity between Voigt 3 and other peaks indicate a very significant additional contribution to Voigt 3. This is interpreted to be the overtone of the water libration band at 804 cm^{-1} and not adsorbed or incorporated non-hydrogen bonded water as suggested by Frost *et al.* (2002).

Supplementary Information References

Al-Borno, A., Tomson, M.B. (1994) The temperature dependence of the solubility product constant of vivianite. *Geochimica et Cosmochimica Acta* 58, 5373–5378. https://doi.org/10.1016/0016-7037(94)90236-4

Bartl, H. (1989) Water of crystallization and its hydrogen-bonded crosslinking in vivianite $Fe_3(PO_4)_2 \cdot 8H_2O$; a neutron diffraction investigation. *Fresenius' Zeitschrift für analytische Chemie* 333, 401–403. https://doi.org/10.1007/BF00572335

Bethke, C.M. (2010) *Geochemical and Biogeochemical Reaction Modeling*. Cambridge University Press, Cambridge.

Capitelli, F., Chita, G., Ghiara, M.R., Rossi, M. (2012) Crystal-chemical investigation of $Fe_3(PO_4)_2 \cdot 8\ H_2O$ vivianite minerals. *Zeitschrift für Kristallographie - Crystalline Materials* 227, 92–101. https://doi.org/10.1524/zkri.2012.1442

Diaz-Moreno, S., Amboage, M., Basham, M., Boada, R., Bricknell, N.E., Cibin, G., Cobb, T.M., Filik, J., Freeman, A., Geraki, K., Gianolio, D., Hayama, S., Ignatyev, K., Keenan, L., Mikulska, I., Mosselmans, J.F.W., Mudd, J.J., Parry, S.A. (2018) The Spectroscopy Village at Diamond Light Source. *Journal of Synchrotron Radiation* 25, 998–1009. https://doi.org/10.1107/S1600577518006173

Frost, R.L., Martens, W., Williams, P.A., Kloprogge, J.T. (2002) Raman and infrared spectroscopic study of the vivianite-group phosphates vivianite, baricite and bobierrite. *Mineralogical Magazine* 66, 1063–1073. https://doi.org/10.1180/0026461026660077

Frost, R.L., Martens, W., Williams, P.A., Kloprogge, J.T. (2003) Raman spectroscopic study of the vivianite arsenate minerals. *Journal of Raman Spectroscopy* 34, 751–759. https://doi.org/10.1002/jrs.1049

Johnston, R.B., Singer, P.C. (2007) Solubility of Symplesite (Ferrous Arsenate): Implications for Reduced Groundwaters and Other Geochemical Environments. *Soil Science Society of America Journal* 71, 101–107. https://doi.org/10.2136/sssaj2006.0023

Kelly, S.D., Hesterberg, D., Ravel, B. (2008) Analysis of soils and minerals using X-ray absorption spectroscopy. In: Ulery, A.L., Drees, L.R. (Eds.) *Methods of Soil Analysis Part 5—Mineralogical methods*. Soil Science Society of America, Madison, WI, 387–463. https://doi.org/10.2136/sssabookser5.5.c14

Kitahama, K., Kiriyama, R., Baba, Y. (1975) Refinement of the crystal structure of scorodite. *Acta Crystallographica Section B: Structural Crystallography and Crystal Chemistry* 31, 322–324. https://doi.org/10.1107/S056774087500266X

Klementiev, K., Chernikov, R. (2016) XAFSmass: A program for calculating the optimal mass of XAFS samples. *Journal of Physics: Conference Series* 712, 012008. https://doi.org/10.1088/1742-6596/712/1/012008

Mikutta, C., Frommer, J., Voegelin, A., Kaegi, R., Kretzschmar, R. (2010) Effect of citrate on the local Fe coordination in ferrihydrite, arsenate binding, and ternary arsenate complex formation. *Geochimica et Cosmochimica Acta* 74, 5574–5592. https://doi.org/10.1016/j.gca.2010.06.024

Momma, K., Izumi, F. (2008) *VESTA*: A three-dimensional visualization system for electronic and structural analysis. *Journal of Applied Crystallography* 41, 653–658. https://doi.org/10.1107/S0021889808012016

Mori, H., Ito, T. (1950) The Structure of Vivianite and Symplesite. *Acta Crystallographica* 3, 1–6. https://doi.org/10.1107/S0365110X5000001X

Muehe, E.M., Morin, G., Scheer, L., Le Pape, P., Esteve, I., Daus, B., Kappler, A. (2016) Arsenic(V) Incorporation in Vivianite during Microbial Reduction of Arsenic(V)-Bearing Biogenic Fe(III) (Oxyhydr)oxides. *Environmental Science & Technology* 50, 2281–2291. https://doi.org/10.1021/acs.est.5b04625

Myneni, S.C.B., Traina, S.J., Waychunas, G.A., Logan, T.J. (1998) Experimental and theoretical vibrational spectroscopic evaluation of arsenate coordination in aqueous solutions, solids, and at mineral-water interfaces. *Geochimica et Cosmochimica Acta* 62, 3285–3300. https://doi.org/10.1016/S0016-7037(98)00222-1

Nakamoto, K. (1986) *Infrared and Raman Spectra of Inorganic and Coordination Compounds*. Wiley, Hoboken, NJ.

Newville, M. (2001) *IFEFFIT*: Interactive XAFS analysis and *FEFF* fitting. *Journal of Synchrotron Radiation* 8, 322–324. https://doi.org/10.1107/S0909049500016964

Paktunc, D., Dutrizac, J., Gertsman, V. (2008) Synthesis and phase transformations involving scorodite, ferric arsenate and arsenical ferrihydrite: Implications for arsenic mobility. *Geochimica et Cosmochimica Acta* 72, 2649–2672. https://doi.org/10.1016/j.gca.2008.03.012

Perez, J.P.H., Freeman, H.M., Schuessler, J.A., Benning, L.G. (2019) The interfacial reactivity of arsenic species with green rust sulfate (GR_{SO4}). *Science of The Total Environment* 648, 1161–1170. https://doi.org/10.1016/j.scitotenv.2018.08.163

Ratajczak, H., Yaremko, A.M. (2000) Theory of profiles of hydrogen stretching infrared bands of hydrogen-bonded solids. Multi-Fermi resonance effects and strong coupling between the high-frequency hydrogen stretching vibration and low-frequency phonons. *Journal of Molecular Structure: THEOCHEM* 500, 413–419. https://doi.org/10.1016/S0166-1280(00)00450-4

Rehr, J.J., Albers, R.C., Zabinsky, S.I. (1992) High-order multiple-scattering calculations of X-ray-absorption fine structure. *Physical Review Letters* 69, 3397–3400. https://doi.org/10.1103/PhysRevLett.69.3397

Socrates, G. (2004) *Infrared and Raman Characteristic Group Frequencies: Tables and Charts*. Third Edition, Wiley, Hoboken, NJ.

Šoptrajanov, B., Jovanovski, G., Pejov, L. (2002) Very low H–O–H bending frequencies. III. Fourier transform infrared study of cobalt potassium phosphate monohydrate and manganese potassium phosphate monohydrate. *Journal of Molecular Structure* 613, 47–54. https://doi.org/10.1016/S0022-2860(02)00130-8

Toby, B.H., Von Dreele, R.B. (2013) *GSAS-II*: The genesis of a modern open-source all purpose crystallography software package. *Journal of Applied Crystallography* 46, 544–549. https://doi.org/10.1107/S0021889813003531

Vandeginste, B.G.M., Massart, D.L., Buydens, L.M.C., De Jong, S., Lewi, P.J., Smeyers-Verbeke, J. (1998) Analysis of Measurement Tables. In: Vandeginste, B.G.M., Massart, D.L., Buydens, L.M.C., De Jong, S., Lewi, P.J., Smeyers-Verbeke, J. (Eds.) *Handbook of Chemometrics and Qualimetrics: Part B*. Elsevier, Amsterdam, 88–104. https://doi.org/10.1016/S0922-3487(98)80041-5

Webb, S.M. (2005) SIXpack: a graphical user interface for XAS analysis using IFEFFIT. *Physica Scripta* 2005, 1011–1014. https://doi.org/10.1238/Physica.Topical.115a01011